Spectroscopic imaging of tin vapor near plasma threshold

D. J. Engels [1,2] H. K. Schubert [1,2] M. Kharbedia [1] W. Ubachs [1,2] and O. O. Versolato [1,2,*]

[1]*Advanced Research Center for Nanolithography, Science Park 106, 1098 XG Amsterdam, The Netherlands*

[2]*Department of Physics and Astronomy and LaserLab, Vrije Universiteit Amsterdam, De Boelelaan 1100, 1081 HZ Amsterdam, The Netherlands*

(Received 14 February 2025; accepted 10 June 2025; published 26 June 2025)

We report on the spectroscopic imaging of tin vapors laser generated from thin liquid tin targets using laser intensities around the threshold of plasma formation. Specifically, we study tin vapor using an extinction imaging method in the UV regime (230–400 nm) to obtain 40-μm spatial-resolution images with 10-cm^{-1}-resolution spectra 100 ns after vaporization. The vapor is created by irradiating a nonoxidized free-flying thin film with a nanosecond laser pulse, the intensity of which is varied between 1 and 130 × 10^7 W/cm^2, from below to above the threshold of producing plasma. Vapors created with laser intensities below 40 × 10^7 W/cm^2 exhibit a spatially homogeneous neutral atomic component, with a temperature around 3000 K, as well as a broadband component due to nanoparticles. The morphology and composition of the vapor change as the plasma forms during vaporization at higher intensities, with the temperature of the vapor rising to 8000 K at the highest intensity. At these intensities, the broadband component disappears, indicating that it is a vapor composed only of free atoms.

DOI: 10.1103/f8l3-cyvx

I. INTRODUCTION

Vapors near plasma formation threshold find applications in high-tech fabrication technologies as well as in next-generation fusion power generation concepts. In pulsed laser deposition [1], as an example of physical vapor deposition techniques [2], an ∼10^9 W/cm^2 laser pulse ablates a target, creating a plasma vapor plume, to deposit thin layers for the fabrication of high-performance multielement coatings. Plasma-assisted atomic layer deposition enables the synthesis of ultrathin films with atomic resolution [3]. In liquid metal divertor technology for nuclear fusion, specifically in "vapor box" concepts, vapor is used to reduce and radiate away [4,5] the heat load on the wall of fusion devices [6–8]. Vapor is also of interest for extreme ultraviolet (EUV) lithography, which uses hot-and-dense tin plasma to produce EUV light [9]. To generate the required light, liquid tin droplets are first preshaped into thin films before being irradiated by the EUV-producing "main pulse" [10–12] (for alternative approaches see, e.g., Refs. [13–18]). Preplasma formation [18–20] and "advanced target shaping" concepts [21] are proposed to extend current preshaping techniques for improved operation efficiency. All such applications benefit from having diagnostics to obtain vapor characteristics and to provide feedback for control loops.

Inspired by these applications, in particular those related to EUV generation, we apply a spectroscopic absorption imaging method following Engels *et al.* [22] to diagnose tin vapor created by irradiating a thin film with a nanosecond laser pulse over a range of intensities spanning (1–130) × 10^7 W/cm^2 around the threshold to produce plasma. Prior work [22] provided a view of the local temperature, composition (i.e., atoms vs nanoparticles), and local densities of such tin vapor at an intermediate laser intensity (∼10^8 W/cm^2) where no plasma was generated. The current range of laser pulse intensities allows us to witness and study in detail the changes in target morphology and composition with laser intensity, ranging from below to above the threshold of producing plasma from the liquid target, and to demonstrate the applicability of the spectroscopic imaging method also in the regime of plasma generation in tin vapor.

II. METHODS

In the experiment (see Fig. 1), a nonoxidized free-flying liquid tin sheet is created in a vacuum by expanding a molten microdroplet using a nanosecond laser pulse. The sheet (the "target") has a diameter of approximately 500 μm with a thickness of 25–10 nm (decreasing radially outward [23]). This target serves the purpose of providing an isolated thin layer of metal and is kept constant throughout the current study (for details on the dynamics of target preparation see Ref. [24], and references therein). To vaporize the target, we employ a vaporization pulse (VP; 6 ns, λ = 1064 nm) focused to a circular spot with a diameter of ∼1.5 mm at the target location (the laser intensity is nearly constant over the sheet, decreasing only ∼5% from the center to the edge). To create different vapors, the intensity of the vaporization pulse is varied over a range (1–130) × 10^7 W/cm^2, keeping all other things constant.

We image the vapor with a UV "shadowgraphy" pulse (SP) at a 90° angle to the VP. The UV pulse has a length of 4 ns,

*Contact author: versolato@arcnl.nl

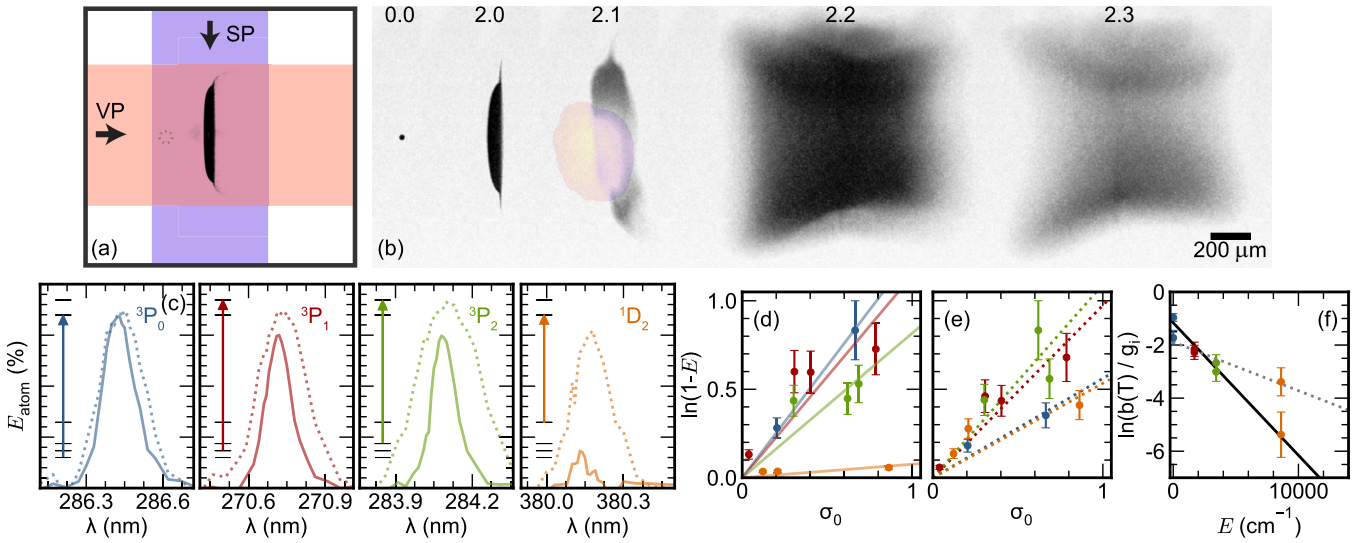

FIG. 1. Setup and methods. (a) The direction of the vaporization pulse (VP; orange) and the perpendicular shadowgraphy pulse (SP; purple) that follows 100 ns later from a top-view perspective. (b) Processed side-view shadowgrams created with 284.08 nm backlighting at different times in the droplet to sheet to vapor process. The VP (here at its highest intensity) arrives 2.1 µs after the droplet is expanded into a sheet. The light produced from plasma generated during the vaporization is highlighted in false color. (c) Extinction (scattering + absorption) around several atomic resonances when the broadband term is subtracted (E_{atom}). The plot colors are related to the ground levels of the resonances (also indicated on the top right). The transition is also shown in a schematic level diagram of ground state tin ($5s^25p^2$) on the left of each resonance. The solid line is the 5×10^7 W/cm^2 case, while the dotted line is the 130×10^7 W/cm^2 case. Note the strongly increased absorption for the highest ground state. (d) σ_0 vs $\ln(1-E)$ integrated over the resonance, for the low-intensity case. See the main text for information. Panel (e) shows the high-intensity case. (f) Boltzmann plot for the two intensities (dotted is the high intensity).

a spectral bandwidth of 5–10 cm^{-1}, and a tunable wavelength between 230 and 400 nm for spectroscopy. Figure 1(b) shows the evolution of the droplet into a thin-film target and, subsequently, into a vapor.

We capture 25 frames at each UV wavelength with a fixed 100 ns delay between the VP and the SP (each frame is a new laser-droplet event). The 100 ns delay between VP and SP is chosen such that the camera exposure start can be placed in between, avoiding plasma emission in the images (which would interfere with the absorption measurements) without the vapor thinning too much and reducing signal to noise. Varying the VP and SP delay would provide further insights on the dynamics of the expanding vapor, such as composition or density changes. Here, we focus on the impact of a single parameter, the VP intensity, with a study of the vapor dynamics left for future work. The ten best-aligned, most up-down-symmetric frames are selected from the 25 frames. Next, they are geometrically overlapped, averaged, and corrected for differences in magnification (which changes with wavelength due to chromatic aberrations of the single-lens imaging setup). Finally, all CCD pixels are binned into 16 by 16 bins (called a pixel hereafter) to prevent the impact of any misalignment, resulting in images without visible "speckle" and improved signal to noise, with an effective resolution of 40 µm.

We determine the vapor temperature, per pixel, via strong Sn-I resonances originating from four electronic levels [see Table I in the Appendix and cf. Fig. 1(c)]. Figure 1(c) shows extinction (scattering + absorption) profiles (for two separate VP intensity cases, dotted and solid lines, respectively) for each of four selected atomic resonances, one from each of the four lowest-lying electronic levels. The broadband contribution is removed from the extinction, yielding E_{atom}. For three of the transitions [cf. Fig. 1(c)], we note a significantly increased absorption for the high-intensity case compared to the low-intensity case, with the difference increasing with the energy of the bottom level. This behavior is indicative of a significant temperature change. To further quantify the temperature and any changes therein, we employ a Boltzmann plotting technique (see, e.g., Ref. [25] for reference) closely following the approach of our previous work [22]. We plot the integral over the wave number (ν) of the logarithm under the atomic resonances $\ln(1 - E_{\text{atom}})$ versus the transition's resonance cross section σ_0. This enables extracting the occupation of each level from the Boltzmann factor $b(T)$:

$$\int -\ln\left[1 - E_{\text{atom}}(\nu)\right] d\nu \propto b(T) n L \sigma_0, \tag{1}$$

where n is the density of the vapor and $b(T)n$ is the density of the absorbing state; L is the path length through the vapor, which with n defines the column density nL. The strength of the resonance is determined by the resonance cross section σ_0. Thus, for a single pixel, we can extract the occupation $b(T)$ from slopes in Figs. 1(d) and 1(e). Finally, by fitting a straight line through the occupation versus the energy of the level, a temperature T is extracted [see Fig. 1(f)].

III. RESULTS

A. Spectroscopy

Figure 2 shows all the created vapors, with VP intensities ranging between 1 and 130×10^7 W/cm^2, increasing from left to right. The top row shows shadowgrams at 254.73 nm (at the center of the atomic resonance; cf. Table I), and visualizes how the shape of the vapor changes when changing the VP intensity. At low intensity [panels (a) and (f)] the vapor has a cone shape [22]. For somewhat higher intensities [panels (k) and (p)], the rim starts vaporizing and contributes to the absorption, as highlighted by the gray cloud near the edges of the shadowgram. At these VP intensities, plasma light emission is particularly noticeable near the center (intentionally filtered out by the camera exposure and hence not visible in the shadowgrams). Finally, in panel (u), plasma forms nearly everywhere on the sheet, creating an additional pressure field that changes the shape of the vapor.

The target has three distinct morphological characteristics following the work of Liu *et al.* [24]. One feature is the "center dot," which usually holds about 10% of the initial droplet mass [24], which would make it ∼2 μm thick. The second is the "rim," which bounds the sheet [24]. The thickness of the rim can be predicted from hydrodynamic arguments to be approximately ∼1 μm in diameter [23]. The thinnest part is the sheet, which averages a thickness of around ∼20 nm. Our observations indicate that plasma first forms on the thickness extrema.

In the experiment, visible light emission is determined to be an indicator of plasma formation (previous experiments have correlated light emission with detected ion current [26]). The first emission of visible light is observed in the 25×10^7 W/cm^2 case (the third column in Fig. 2), on the center dot, the thickest part of the target [24]. At 40×10^7 W/cm^2, the fourth column in Fig. 2, plasma also forms on the rim. Only at the final intensity does plasma form on the entire thin film. A detailed study of the plasma formation process itself lies beyond the scope of the present study; in the current work, we focus on the impact of the plasma on the characteristics of the generated vapor.

The second row of Fig. 2 shows the extinction spectrum, expressed as $-\ln(1-E)$ in order to have a value linear with column density nL. The four spectra in each panel correspond to the four pixels shown in the first row. The different pixel locations exhibit nearly identical spectra except for a difference in overall amplitude, which reflects different column densities. Panel (g) shows spectra taken at a VP intensity similar to that of Ref. [22], which indeed are nearly identical [we plot averaged data from Ref. [22] in panel (h)], highlighting the reproducibility of the vapor composition for similar intensities and target shapes (the current target, however, is approximately 2 times thinner). The neighboring panels (b) and (l) show very similar spectra with only an overall change in absorption, even though the VP intensity has changed by a factor of 25. Further increasing the VP intensity leads to clear changes in the spectra, with panels (q) and (v) depicting a decrease and, finally, the disappearance of the "broadband" component previously hypothesized [22] to be caused by Mie scattering by nanoparticles.

To more clearly show the change in the broadband component, we invert Beer-Lambert's law to an equation for the cross section:

$$\sigma(\nu) = -\frac{\ln[1-E(\nu)]}{nL}. \tag{2}$$

The absolute column density nL cannot be directly determined from the experiments without a detailed model for the cross section σ, which necessarily would need to include physical effects such as power, collisional, and Stark broadening. Following Ref. [22], we instead introduce a dimensionless parameter a to describe a "relative density," enabling the comparison of densities within a vapor and also between the various vapors in the experiment. We note that this relative density is a measure of nL and, thus, is a relative *column* density as it includes the path length L.

We obtain the values for a via two complementary methods. The first method is to compare the extinction of the broadband component, resulting in a value for a defined by the Mie scattering component from fitting the spectrum over every pixel to the reference pixel:

$$\min_{a_{\mathrm{Mie}}\in\mathbf{R}} \left| a_{\mathrm{Mie}}\{\ln[1-E_{\mathrm{Mie}}(\nu)]\} - \ln\left[1-E^{\mathrm{ref}}_{\mathrm{Mie}}(\nu)\right]\right|. \tag{3}$$

Note that a_{Mie} (and also a_{atom} below) is a scalar independent of ν. Having obtained a_{Mie}, we can rewrite Eq. (2) with only known parameters

$$\sigma_{\mathrm{rel}}(\nu) = -\frac{\ln[1-E(\nu)]}{a}\frac{1}{\ln(1-\tilde{E})}, \tag{4}$$

with a single normalization applied to all intensity cases at $\tilde{E} \equiv E^{\mathrm{ref}}(\nu = 42\,000\ \mathrm{cm}^{-1})$ from a single pixel [near the blue pixel indicated in Fig. 2(f)] in the 5×10^7 W/cm^2 case enabling the direct comparison to Ref. [22]. The rewriting of the equation allows us to show how the cross section changes over wavelength, regardless of the density-length scale product. This evolution is especially important in Mie theory, where the evolution of the cross section with wavelength is solely determined by the nanoparticle size (together with the refractive index). The resulting relative cross section σ_{rel} is shown in the third row of Fig. 2. The atomic resonances are filtered out to focus on the broadband component of the spectrum. Again, the results of selected pixels (cf. Fig. 2, row 1) are shown, along with two gray bounds (dark and light gray) indicating the 1 and 3 sigma spread for *all* the pixels in the vapor, respectively. Panels (c), (h), and (m) show nearly identical curves, indicating that all pixels in the vapor have the same nanoparticle size distribution underlying this broadband spectrum. The gray bounds are very small, indicating a particular uniformity of the size distribution throughout the vapor. We note that this uniformity holds over a 25 times change in VP intensity. The uniformity breaks down in Fig. 2(r) at 40×10^7 W/cm^2. Although the same trend in the broadband spectrum is still visible, the variation in vapor increases significantly, as indicated by the much larger gray bound [cf. Figs. 2(m) and 2(r)]. Finally, for the highest intensity case [Fig. 2(w)] the broadband component disappears completely. The inset (z) presents a close-up view of panel (w) with the same data (10× zoom on the y axis) and clearly shows that the broadband is negligible. Thus, it appears that the

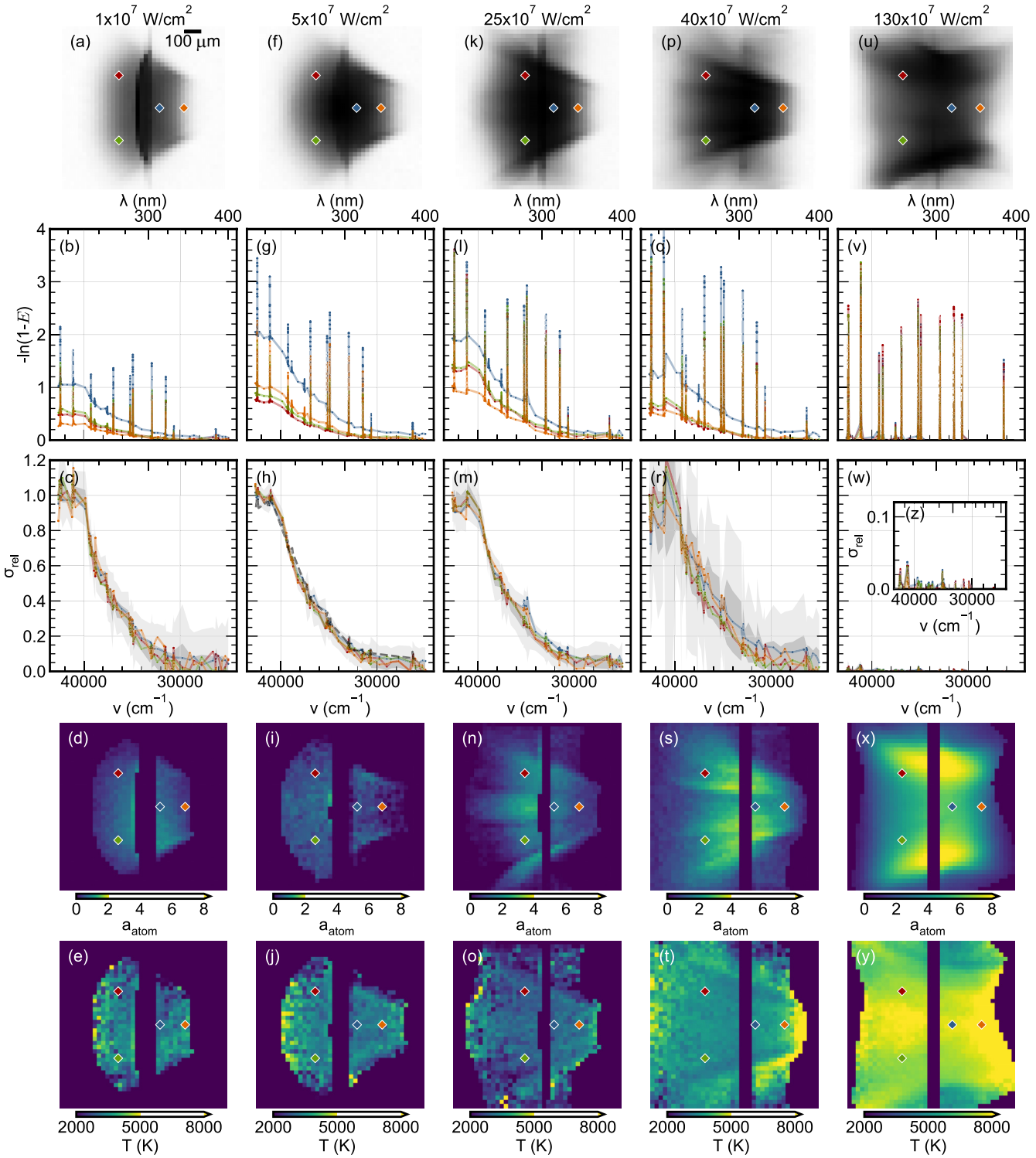

FIG. 2. Analysis of tin vapors at five laser vaporization intensities. Row 1 shows shadowgrams of the relatively weak 254.73 nm atomic resonance ($5s^2 5p^2\ ^3P_0$; see Table I), showing detailed structures in the atomic vapor cloud and highlighting the shape change of the vapor with VP intensity. Row 2 shows the extinction spectra for the four highlighted locations in row 1. Row 3 shows the relative cross section (σ_{rel}) for the four locations (the atomic resonances are filtered out). We also indicate the spread over all the pixels (at 1 and 3 standard deviations; gray shading). Panel (h), which closely matches previously published data (see the main text), also shows (gray dashed line) the previously published mean for all pixels for comparison. Row 4 shows the relative, unitless, densities a_{atom} determined using the atomic resonances. Pixels where no value could be determined are colored dark blue. Row 5 shows the temperature maps for each intensity.

nanoparticles deemed responsible for the background component have disappeared completely.

Given that the broadband component is absent at the highest intensity, it is advantageous to instead define a via the atomic resonances, which are still very much present in this highest intensity case. We sum over a full atomic resonance (to accommodate varying broadening effects due to varying density) to obtain an integrated line strength. By comparing the line strengths for different pixels, we again obtain a value for a much like Eq. (3):

$$a_{\mathrm{atom}} = \frac{\sum^{n_{\mathrm{peaks}}} \sum_{\nu_{\mathrm{min}}}^{\nu_{\mathrm{max}}} \ln\left[1 - E_{\mathrm{atom}}(\nu)\right]}{\sum^{n_{\mathrm{peaks}}} \sum_{\nu_{\mathrm{min}}}^{\nu_{\mathrm{max}}} \ln\left[1 - E^{\mathrm{ref}}_{\mathrm{atom}}(\nu)\right]}, \tag{5}$$

where ν_{max} and ν_{min} are 0.4 nm around each atomic resonance [cf. Fig. 1(c) for an example of the summation range]. Previous work [22] demonstrated that the two methods to obtain a representative relative density a provide nearly identical values, with the a_{Mie} exhibiting a better signal-to-noise ratio and having the advantage of being insensitive to complex atomic broadening dynamics. Hence, we use a_{Mie} to collapse σ_{rel} in panels (c), (h), (m), and (r); for the highest intensity case (w) we resort to using a_{atom}. The values for a_{atom} are of particular interest for a consistent interpretation of the spatial changes in the relative density when varying the intensity of the VP in the following.

B. Imaging

Our spectroscopic imaging method enables us to spatially characterize the relative densities for the various VP intensities used. The fourth row in Fig. 2 shows the determined values of a_{atom} for each pixel. Similarly to σ_{rel}, the relative density a_{atom} is normalized by its value for the same single pixel in the 5×10^7 W/cm^2 case. This single normalization enables the direct comparison of the relative densities between all the VP intensities used. In general, a trend to higher values for a_{atom} is observed as intensity increases. In part, this trend is explained by more vaporized mass as the fluence increases with intensity. We note that the rim and center mass hold nearly as much mass as the sheet itself for this target [23] and continue to be a source of atoms. Another factor in explaining the observed trend may be the redistribution of the vapor mass constituents, as the broadband component due to nanoparticles disappears and this mass shows up as free atoms. This mass redistribution is clearest in Fig. 2(x), the highest intensity case, without a broadband component in the spectra, where the values for a_{atom} have risen to about eight times the value of panel (i). The highest values for a_{atom} are near the edges of the vapor, likely originating from the thick rim, a source of many atoms at high fluences.

We can also employ the Boltzmann plotting method for each pixel at each intensity. The final row shows the resulting temperature maps. The first four intensities [Figs. 2(e), 2(j), 2(o), and 2(t)] do not deviate significantly from an ~3000 K temperature in the vapor, near the boiling point of tin (at 2875 K). However, the temperature jumps to around 8000 K for the final intensity in panel (y). The hottest area seems to be around the center. This could be explained by the presence of the center dot feature here, which is the thickest and thus sustains a plasma the longest before vaporizing.

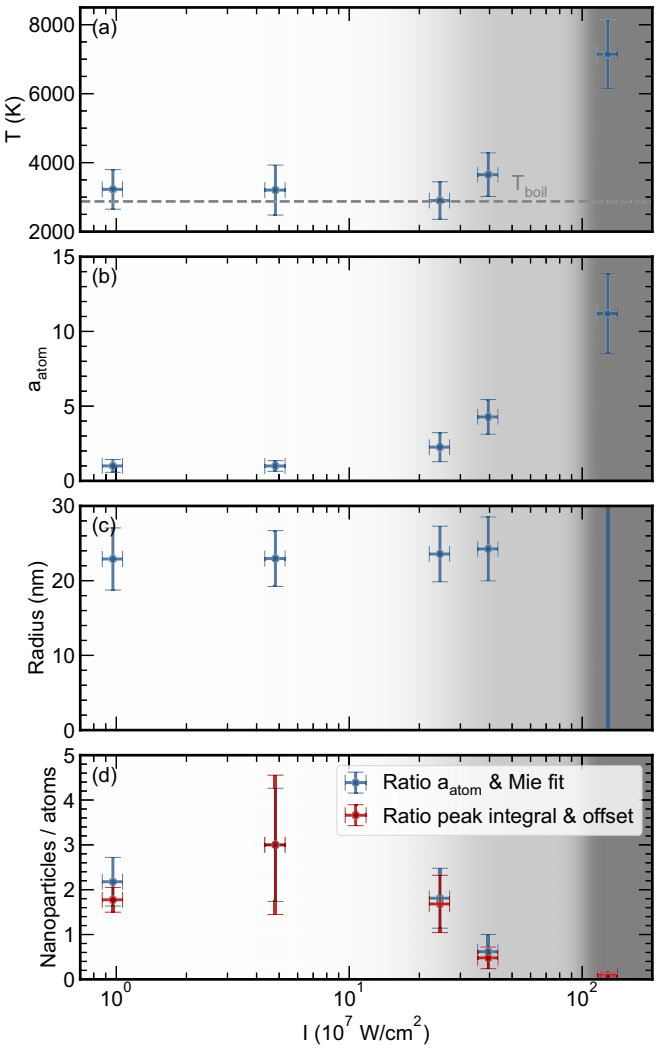

FIG. 3. Key parameters over VP intensity. (a) The temperature of the vapor. The boiling temperature (2875 K) is also indicated. The gray-shaded background indicates whether plasma forms on the thin film. In the light-gray area, the intensity is high enough to form plasma on the "thick" features of the target, such as the center dot and rim. In the dark-gray area, plasma forms on the entire thin film. We plot the mean and spread over all pixels as an error bar. (b) The relative density of the atoms a_{atom}. (c) The fitted nanoparticle radius. A fit is performed per pixel. (d) The mass ratio of nanoparticles and atoms. This value is set to three at 5×10^7 W/cm^2 (matching previously published work) [22].

C. Scaling of key parameters

We leave behind the imaging and investigate key parameters of the vapor over the 2 orders of magnitude change in VP intensity. In Fig. 3, we plot the mean and spread over *all* pixels for the various parameters as a function of laser intensity.

First, we show the extracted temperature in Fig. 3(a) as it rises from the boiling temperature towards 8000 K. The rather sudden temperature increase is observed to coincide

with the formation of plasma. In panel (a), the light-gray background represents the onset of plasma on the thicker parts of the target (being the rim and center dot), while the dark-gray area indicates the intensity region at which plasma is seen to form everywhere on the sheet. These regions are also indicated in panels (b)–(d). Next, we show the change in the relative density a_{atom} in Fig. 3(b). Starting around 1 ($a_{\text{atom}} = 1$ is defined for a pixel in the 5×10^7 W/cm^2 case), the relative density increases with the laser intensity. The large monoatomic vapors created with high VP intensities could be excellent targets to effectively absorb a following (main) laser pulse in EUV lithography, as such vapors offer a long path length of absorbers.

Next, we turn toward the broadband part of the spectrum, which is associated with scattering from nanoparticles. Comparing Figs. 2(m), 2(r), and 2(w), we observe a strong reduction in this broadband part of the spectrum, indicating that the nanoparticles disappear at the highest intensity. To quantify the change in the composition of the vapor, we fit each spectrum per pixel (after filtering out the atomic resonances) with the extinction curve predicted by Mie theory. We use a numerical code [27] for Mie theory and use as input the refractive index data from Cisneros *et al.* [28], extrapolated to wavelengths below 310 nm using a Drude-model fit. This fit results in a column density and a best-fit nanoparticle size for each pixel.

In Fig. 3(c), we show the result of these fits by showing the mean and spread of the nanoparticle size. At low intensities, the nanoparticle radius obtained from the fit is nearly constant, around 23 nm, in line with the finding of Ref. [22] that the radii are at, or below, the 25 nm level. However, as plasma is formed at the highest intensity, the fit fails (indicated by the vertical blue line) due to the negligible remaining signal in the broadband curve. We note that the Mie theory fit carries significant uncertainties due to the work function of tin being passed around 280 nm (thus allowing ionization of clusters) and the fact that we extrapolate the refractive index below 310 nm.

We now focus on the column density of the nanoparticles. We obtain this value (in nanoparticles per volume) from the same fit for each pixel and convert it into atoms in nanoparticles per volume. Having obtained this value for each pixel, we now have a value for the change in atomic density (our relative atomic density a_{atom}) and a value for the change in nanoparticle density. With both of these, we can determine how the ratio of atoms contained in nanoparticles versus free atoms changes with VP intensity and show the results in Fig. 3(d). We set the ratio of nanoparticles versus atoms to 3 at the 5×10^7 W/cm^2 intensity, using input from Ref. [22] as a reference value. A clear downward trend of the ratio with increasing laser intensity is observed. The uncertainty is dominated by the uncertainty in the nanoparticle size, but also includes a measure of the spatial variation throughout the vapor.

We next confirm this trend in the ratio by introducing a second metric that has no model dependence. Here, we compare the integral under the 235 nm atomic resonance (see Table I; this resonance has the highest broadband baseline) to its broadband baseline, caused by the nanoparticles. Thus, by tracking how the ratio of the integral of E_{atom} and the baseline changes, we obtain a proxy for the bound-to-free-atom ratio. These results are shown in Fig. 3(d) in red. Again, we fix the resulting ratio to 3 at the 5×10^7 W/cm^2 intensity. This independent, model-free approach closely matches that of the Mie fit and enables us to conclude that the ratio strongly decreases with the VP intensity to create a nearly pure atomic vapor at the highest VP intensity, effectively transferring mass from bound to free atoms and increasing atomic absorption [cf. Figs. 2(i)–2(x)].

Overall, we have shown that the various vapors are quite similar, with respect to their spectral and spatial aspects, over the intensity range 1×10^7 W/cm^2 to 25×10^7 W/cm^2. This similarity indicates that vaporization in this intensity range is governed by the same physical processes as those identified by Schubert *et al.* [29] given the partial overlap on the lower end of the studied intensity range (0.2×10^7 W/cm^2 to 4×10^7 W/cm^2 in Ref. [29]). The dissimilarity of the vapor at the highest intensity, in particular the absence of broadband absorption, indicates that a different physical process starts to contribute. It remains an open question what is the exact process that causes the transition to a nearly pure atomic vapor at the highest intensity, around the plasma threshold. We hypothesize that plasma prevents the formation of clusters from the flux of free atoms coming from the liquid surface [29]. However, to prove this decisively versus an alternative hypothesis such as plasma-induced atomization of clusters, further studies are required.

IV. CONCLUSION

In this work, we report on the spectroscopic imaging of pure metallic tin vapors generated from thin liquid tin targets over a range of intensities of the vaporizing laser pulse, from below to above the threshold of producing plasma. We show that vapors created with laser intensities below 40×10^7 W/cm^2 consist of a spatially homogeneous atomic component, with a temperature around 3000 K, and a strong broadband component due to nanoparticles. The vapor morphology and composition change considerably as plasma forms at higher intensities, with the temperature rising to 8000 K at the highest intensity. Here, the broadband component completely disappears, indicating that the vapor is composed of free atoms only. With the current studies, we demonstrate the applicability of the spectroscopic imaging method also in the regime of plasma generation.

ACKNOWLEDGMENTS

The authors thank Michael Purvis and Haining Wang for valuable discussions and ASML for loaning a laser system. We would also like to thank Henk-Jan Boluijt and Laurens van Buuren for their work on the experimental setup and Jorijn Kuster for his work on the acquisition software. This work was conducted at the Advanced Research Center for Nanolithography (ARCNL), a public-private partnership between the University of Amsterdam (UvA), Vrije Universiteit Amsterdam (VU), Rijksuniversiteit Groningen (UG), the Dutch Research Council (NWO), and the semiconductor equipment manufacturer ASML and was partly financed by "Toeslag

voor Topconsortia voor Kennis en Innovatie (TKI)" from the Dutch Ministry of Economic Affairs and Climate Policy. This publication is also a part of the project "Plasma driven by a variable-wavelength laser for next-generation EUV sources for nanolithography" (with project No. 19458) of the Open Technology Programme, which is financed by NWO.

The authors have no conflicts to disclose.

DATA AVAILABILITY

The data that support the findings of this article are not publicly available upon publication because it is not technically feasible and/or the cost of preparing, depositing, and hosting the data would be prohibitive within the terms of this research project. The data are available from the authors upon reasonable request.

APPENDIX: ATOMIC RESONANCE OVERVIEW

An overview of all measured atomic transitions is presented below in Table I.

TABLE I. An overview of the measured atomic transitions for neutral tin [30]. Vacuum wavelengths are used.

λ (nm)	Einstein coefficient (1/s)	Transition	Level energies (cm^{-1})
235.56	1.70×10^8	$5p^2\,{}^3P_1$-$5p5d\,{}^3D_2$	1692–44144
242.24	2.50×10^8	$5p^2\,{}^1D_2$-$5p5d\,{}^1F_3$	8613–49893
243.02	1.50×10^8	$5p^2\,{}^3P_2$-$5p5d\,{}^3F_3$	3428–44576
254.73	2.10×10^7	$5p^2\,{}^3P_0$-$5p6s\,{}^1P_1$	0000–39257
257.24	4.50×10^7	$5p^2\,{}^1D_2$-$5p5d\,{}^3D_3$	8613–47488
266.20	1.10×10^7	$5p^2\,{}^3P_1$-$5p6s\,{}^1P_1$	1692–39257
270.73	6.60×10^7	$5p^2\,{}^3P_1$-$5p6s\,{}^3P_2$	1692–38629
284.08	1.70×10^8	$5p^2\,{}^3P_2$-$5p6s\,{}^3P_2$	3428–38629
286.42	5.40×10^7	$5p^2\,{}^3P_0$-$5p6s\,{}^3P_1$	0000–34914
303.50	2.00×10^8	$5p^2\,{}^3P_1$-$5p6s\,{}^3P_0$	1692–34641
317.60	1.00×10^8	$5p^2\,{}^3P_2$-$5p6s\,{}^3P_1$	3428–34914
326.33	2.70×10^8	$5p^2\,{}^1D_2$-$5p6s\,{}^1P_1$	8613–39257
380.21	2.80×10^7	$5p^2\,{}^1D_2$-$5p6s\,{}^3P_1$	8613–34914

[1] H.-U. Krebs, M. Weisheit, J. Faupel, E. Süske, T. Scharf, C. Fuhse, M. Störmer, K. Sturm, M. Seibt, H. Kijewski, D. Nelke, E. Panchenko, and M. Buback, Pulsed laser deposition (PLD)–a versatile thin film technique, in *Advances in Solid State Physics*, edited by B. Kramer (Springer, Berlin, Heidelberg, 2003), pp. 505–518.

[2] S. M. Rossnagel, Thin film deposition with physical vapor deposition and related technologies, J. Vac. Sci. Technol. A **21**, S74 (2003).

[3] H. B. Profijt, S. E. Potts, M. C. M. Van De Sanden, and W. M. M. Kessels, Plasma-assisted atomic layer deposition: Basics, opportunities, and challenges, J. Vac. Sci. Technol. A **29**, 050801 (2011).

[4] G. G. Van Eden, T. W. Morgan, D. U. B. Aussems, M. A. Van Den Berg, K. Bystrov, and M. C. M. Van De Sanden, Self-regulated plasma heat flux mitigation due to liquid Sn vapor shielding, Phys. Rev. Lett. **116**, 135002 (2016).

[5] G. G. Van Eden, V. Kvon, M. C. M. Van De Sanden, and T. W. Morgan, Oscillatory vapour shielding of liquid metal walls in nuclear fusion devices, Nat. Commun. **8**, 192 (2017).

[6] T. W. Morgan, P. Rindt, G. G. van Eden, V. Kvon, M. A. Jaworksi, and N. J. Lopes Cardozo, Liquid metals as a divertor plasma-facing material explored using the pilot-PSI and magnum-PSI linear devices, Plasma Phys. Control. Fusion **60**, 014025 (2018).

[7] S. Roccella, G. Dose, R. de Luca, M. Iafrati, A. Mancini, and G. Mazzitelli, CPS based liquid metal divertor target for EU-DEMO, J. Fusion Energy **39**, 462 (2020).

[8] P. Rindt, J. L. van den Eijnden, T. W. Morgan, and N. J. Lopes Cardozo, Conceptual design of a liquid-metal divertor for the european DEMO, Fusion Eng. Des. **173**, 112812 (2021).

[9] O. O. Versolato, Physics of laser-driven tin plasma sources of EUV radiation for nanolithography, Plasma Sources Sci. Technol. **28**, 083001 (2019).

[10] K. Nishihara *et al.*, Plasma physics and radiation hydrodynamics in developing an extreme ultraviolet light source for lithography, Phys. Plasmas **15**, 056708 (2008).

[11] H. Mizoguchi, H. Nakarai, T. Abe, K. M. Nowak, Y. Kawasuji, H. Tanaka, Y. Watanabe, T. Hori, T. Kodama, Y. Shiraishi, T. Yanagida, G. Soumagne, T. Yamada, T. Yamazaki, and T. Saitou, High power LPP-EUV source with long collector mirror lifetime for high volume semiconductor manufacturing, in *2018 China Semiconductor Technology International Conference (CSTIC)* (IEEE, Shanghai, 2018), pp. 1–7.

[12] I. Fomenkov *et al.*, Light sources for high-volume manufacturing EUV lithography: Technology, performance, and power scaling, Adv. Opt. Technol. **6**, 173 (2017).

[13] D. Hudgins, N. Gambino, B. Rollinger, and R. Abhari, Neutral cluster debris dynamics in droplet-based

laser-produced plasma sources, J. Phys. D: Appl. Phys. **49**, 185205 (2016).

[14] D. Hudgins and R. S. Abhari, Rupture time of droplets impacted by a burst of picosecond laser pulses, Phys. Rev. E **99**, 031102 (2019).

[15] A. Hassanein, T. Sizyuk, V. Sizyuk, and S. S. Harilal, Combined effects of prepulsing and target geometry on efficient extreme ultraviolet production from laser produced plasma experiments and modeling, J. Micro/Nanolith. MEMS MOEMS **10**, 033002 (2011).

[16] S. Yu. Grigoryev, B. V. Lakatosh, M. S. Krivokorytov, V. V. Zhakhovsky, S. A. Dyachkov, D. K. Ilnitsky, K. P. Migdal, N. A. Inogamov, A. Yu. Vinokhodov, V. O. Kompanets, Yu. V. Sidelnikov, V. M. Krivtsun, K. N. Koshelev, and V. V. Medvedev, Expansion and fragmentation of a liquid-metal droplet by a short laser pulse, Phys. Rev. Appl. **10**, 064009 (2018).

[17] P. Koukouvinis, N. Kyriazis, and M. Gavaises, Smoothed particle hydrodynamics simulation of a laser pulse impact onto a liquid metal droplet, PLoS One **13**, e0204125 (2018).

[18] V. Sizyuk, T. Sizyuk, and A. Hassanein, Temporal pre-pulse shaping in dual pulse laser produced plasma for the optimization of the EUV source in tin microdroplet system, J. Appl. Phys. **135**, 093101 (2024).

[19] J. R. Freeman, S. S. Harilal, and A. Hassanein, Enhancements of extreme ultraviolet emission using prepulsed Sn laser-produced plasmas for advanced lithography applications, J. Appl. Phys. **110**, 083303 (2011).

[20] T. Cummins, C. O'Gorman, P. Dunne, E. Sokell, G. O'Sullivan, and P. Hayden, Colliding laser-produced plasmas as targets for laser-generated extreme ultraviolet sources, Appl. Phys. Lett. **105**, 044101 (2014).

[21] I. Fomenkov, EUV source for high volume manufacturing: Performance at 250 W and key technologies for power scaling, in *EUV Source Workshop* (2017), https://euvlitho.com/2017/S1.pdf.

[22] D. J. Engels, R. A. Meijer, H. K. Schubert, W. J. van der Zande, W. Ubachs, and O. O. Versolato, High-resolution spectroscopic imaging of atoms and nanoparticles in thin film vaporization, Appl. Phys. Lett. **123**, 254102 (2023).

[23] B. Liu, D. Kurilovich, H. Gelderblom, and O. O. Versolato, Mass loss from a stretching semitransparent sheet of liquid tin, Phys. Rev. Appl. **13**, 024035 (2020).

[24] B. Liu, R. A. Meijer, W. Li, J. Hernandez-Rueda, H. Gelderblom, and O. O. Versolato, Mass partitioning in fragmenting tin sheets, Phys. Rev. Appl. **20**, 014048 (2023).

[25] H.-J. Kunze, *Introduction to Plasma Spectroscopy* (Springer Science & Business Media, Berlin, 2009), Vol. 56.

[26] L. Poirier, D. J. Hemminga, A. Lassise, L. Assink, R. Hoekstra, J. Sheil, and O. O. Versolato, Strongly anisotropic ion emission in the expansion of Nd:YAG-laser-produced plasma, Phys. Plasmas **29**, 123102 (2022).

[27] S. Prahl, Miepython—miepython 2.2.3 documentation, https://miepython.readthedocs.io/en/v2.2.3/index.html.

[28] G. Cisneros, J. S. Helman, and C. N. J. Wagner, Dielectric function of liquid tin between 250 and 1100 °C, Phys. Rev. B **25**, 4248 (1982).

[29] H. K. Schubert, D. J. Engels, R. A. Meijer, B. Liu, and O. O. Versolato, Scaling relations in laser-induced vaporization of thin free-flying liquid metal sheets, Phys. Rev. Res. **6**, 023182 (2024).

[30] A. Kramida, Yu. Ralchenko, J. Reader, and NIST ASD Team, NIST Atomic Spectra Database (ver. 5.10), https://physics.nist.gov/asd.